Going Above and Beyond: A Tenfold Gain in the Performance of Luminescence Thermometers Joining Multiparametric Sensing and Multiple Regression

*Fernando E. Maturi,[1,2] Carlos D. S. Brites,[1] Erving C. Ximendes,[3] Carolyn Mills,[4] Bradley Olsen,[4] D. Jaque,[3] Sidney J. L. Ribeiro,[2] and Luís D. Carlos[1]**

[1]Phantom-g, CICECO – Aveiro Institute of Materials, Department of Physics, University of Aveiro, 3810–193 Aveiro, Portugal
[2]Institute of Chemistry, São Paulo State University (UNESP), Araraquaram, SP 14800–060, Brazil
[3]Nanomaterials for Bioimaging Group, Universidade Autónoma de Madrid, Madrid 28049, Spain
[4]Department of Chemical Engineering, Massachusetts Institute of Technology, Cambridge, MA 02139, USA

*E-mail: lcarlos@ua.pt

Keywords: luminescence nanothermometry, multiple linear regression, green fluorescent protein, silver sulfide

Luminescence thermometry has substantially progressed in the last decade, rapidly approaching the performance of concurrent technologies. Performance is usually assessed through the relative thermal sensitivity, S_r, and temperature uncertainty, δT. Until now, the state-of-the-art values at ambient conditions do not exceed maximum S_r of 12.5% K^{-1} and minimum δT of 0.1 K. Although these numbers are satisfactory for most applications, they are insufficient for fields that require lower thermal uncertainties, such as biomedicine. This has motivated the development of materials with an improved thermal response, many of them responding to the temperature through distinct photophysical properties. This paper demonstrates how the performance of multiparametric luminescent thermometers can be further improved by simply applying new analysis routes. The synergy between multiparametric readouts and multiple linear regression makes possible a ten fold improvement in S_r and δT, reaching a world record of 50% K^{-1} and 0.05 K, respectively. This is achieved without requiring the development of new materials or upgrading the detection system as illustrated by using the green fluorescent protein and Ag_2S nanoparticles. These results open a new era in biomedicine thanks to the development of new diagnosis tools based on the detection of super-small temperature fluctuations in living specimens.

1. Introduction

Temperature is a physical quantity that measures the thermal energy of a body,[1] and temperature fluctuations play a central role in a myriad of natural and man-made processes.[2–4] Since the time-response of a thermometer is limited by its size, the real-time measurement of temperature at the microscopic scale is hindered by the dimensions of the thermal probe. The size effect motivates the development of novel solutions for temperature determination at the sub-micrometric scale. Luminescent nanothermometry is based on the emission properties of luminescent nanomaterials and thus allows remote temperature detection, virtually improving spatial and temporal resolutions in comparison with the macroscopic counterparts.[5–11]

There are plenty of luminescent materials used as nanothermometers, *e.g.*, polymers,[12,13] organic dyes,[14] proteins,[15] quantum dots (QDs),[16,17] and lanthanide-doped particles.[18–21] Different classes of nanothermometers exploit distinct photophysical properties of the emitting center, such as the integrated emission intensity of a single transition,[22] the intensity ratio of two emission bands,[23,24] the energy shift[25] or the bandwidth of an emission line,[26,27] the polarization state of the emission,[28] or the emission lifetime of an excited state.[29] Irrespectively of the property analyzed, all these examples are based on a thermometric parameter (usually denoted by Δ), that expresses the relationship between the luminescent property to be analyzed and the temperature.[7]

The different thermometric parameters reported motivated the community to adopt a figure of merit able to compare the performance of distinct luminescent nanomaterials regardless of the thermometric parameter used.[30,31] This is the so-called relative thermal sensitivity, $S_r = \frac{1}{\Delta}\left|\frac{\partial \Delta}{\partial T}\right|$,[32] where $\partial\Delta/\partial T$ is the change of Δ with respect to the temperature (so-called absolute sensitivity, S_a), with S_r values commonly presented in units of percentage change per degree of temperature change ($\%\cdot K^{-1}$).[5] Up to now, the most sensitive luminescent nanothermometer reported at ambient conditions reaches a maximum value of S_r, represented by S_m, of 12.5 $\%\cdot K^{-1}$.[33]

In the past years, luminescence nanothermometry has been used in both applied and fundamental science. In nanomedicine, for example, the accurate determination of the temperature can yield the development of new thermal diagnosis and therapy methods,[8,11,34] whereas in micro or nanoelectronics tracking the thermal exchanges at submicrometric length scales can afford a detailed understanding of the thermal properties in spatial domains for which the macroscopic transfer laws are not valid anymore.[35] In fact, real-world applications of luminescence thermometry are hindered by the accuracy of the nanothermometers, which is given by the temperature uncertainty, $\delta T = \frac{1}{S_r}\frac{\delta\Delta}{\Delta}$,[7] where $\delta\Delta/\Delta$ is the relative uncertainty in Δ, determined by the detection system used. The best δT value reported by now was achieved by using lanthanide-bearing nanomaterials, ranging between 0.1 and 0.3 K.[4,20]

Nowadays, cutting-edge reports on luminescence nanothermometry are reaching the boundary of the accuracy of the nanothermometers.[11,36] Therefore, the development of new approaches to obtain low-uncertainty luminescent thermal probes is highly demanded to push the field forward, mainly for *in vitro* and *in vivo* thermal sensing.[37,38] Two strategies are envisaged to decrease δT. The first one is the design of high-sensitive light detectors and brighter materials to achieve a higher signal-to-noise ratio, consequently decreasing $\delta\Delta/\Delta$. The second one relies on the improvement of S_r, which can be attained either through the fabrication of new materials or the design of new strategies to define the thermometric parameter. In this work, we are addressing this latter approach.

Recently, the reliability of luminescent nanothermometers has been improved using the combination of distinct thermometric parameters.[39–41] This strategy is based on the use of the so-called multi-parametric nanothermometers in which temperature impacts, simultaneously, on different luminescence properties. The capability of providing different thermal readouts allows improving the reliability in measurements of temperature by providing self-calibrated nanothermometers, increasing the precision of temperature measurements.[33,40,42]

Multiparametric nanothermometers are gaining special attention in biomedicine: Ag_2S nanocrystals have demonstrated their potential for reliable thermal sensing in small animal models,[43,44] whereas the multi-faced changes in the band-shape of green fluorescent protein (GFP) can be used for temperature sensing and imaging in cell biology and physiology.[15,28,45–48] Despite it helps to improve the reliability, the so-called multiparameter sensing is still unable to improve significantly the relative thermal sensitivity of the nanothermometers and the reported values are far below the most sensitive luminescent thermometers reported so far.[33,49,50]

Multiple linear regression (MLR) is an ingenious method to fully expand the potential of multiparameter temperature sensing, which may raise the luminescence nanothermometry to a whole new level. In its easier form, MLR is a powerful tool that evaluates the impact of multiple independent variables on a single experimental outcome quantity.[51] This technique is widely employed in economics to forecast the price of oil[52] or cryptocurrencies,[53] in social sciences to identify fake news[54] and political trends,[55] in medicine to predict blood glucose[56] and cholesterol[57] in overweight patients, and chemistry to quantify metabolites[58] and proteins[59] by mass spectrometry. By analogy, if a luminescent nanothermometer presents different thermometric parameters displaying the same temperature-dependent linear trend, the application of MLR to its multiple thermal reading would lead to a relevant improvement in its performance as a temperature sensor. This possibility has never been proposed neither demonstrated.

Therefore, here, we provide experimental evidence of how the synergy between MLR and multi-parametric thermal sensing leads to a 10-fold improvement in the performance of multi-parametric nanothermometers establishing world-record values for S_r and δT. This is demonstrated by selecting enhanced GFP (EGFP) and Ag_2S nanocrystals as paradigmatic multiparametric thermographic phosphors displaying distinct (and independent) temperature-dependent parameters. *In vivo* experiments involving Ag_2S nanocrystals were revisited

illustrating the impact of this new methodology on the potential application of luminescent nanothermometry in biomedicine.

2. Results

2.1. Multiparametric nanothermometry using EGFP.

Figure 1 shows the temperature-dependent emission spectra of EGFP displaying a significant thermal quenching due to the enhancement of nonradiative decays upon heating.[60,61] The detailed analysis of the band-shape shows that measurable changes are seen after the spectral deconvolution (see Section S1.3 of the Supporting Information), revealing that temperature impacts on several parameters such as the intensity ratio of the integrated areas of peaks 1 and 2 ($I_R = A_1/A_2$), peak energy of both peaks (E_1 and E_1), and their respective full width at half maximum (W_1 and W_2). Each of these parameters can be used as independent Δ values for multiparametric thermal reading (Figure 1d-h) and as their temperature dependencies are described by a single linear fit with a positive correlation there are five reliable independent pathways for determining the temperature from EGFP in a single experiment. At ambient conditions, I_R, E_1, E_2, W_1 and W_2 present S_m values of 0.17, 1.6×10^{-2}, 2.1×10^{-2}, 0.33, and 0.10 $\%\cdot K^{-1}$, respectively. These values are within the same thermal sensitivity range that the previously reported nanothermometry data of other EGFP-like proteins (**Table 1**).

We can argue that larger S_r values can be obtained by choosing the energy shift of each peak as thermometric parameters instead of the corresponding peak energies (since S_r depends on $1/\Delta$). However, and although the energy shift was used both in Raman[62,63] and luminescence[64,65] thermometry, we adopt here the peak energy as a thermometric parameter because is still the largest reported value. Nevertheless, the pros and cons of using peak energy and energy shift as thermometric parameters are discussed in detail in Section 1.3.3.1 (Supporting Information).

Once all the five thermometric parameters defined for EGFP display the same linear temperature dependence, it is possible to further improve S_r and δT by treating the data through the MLR approach. If a nanothermometer displays distinct thermometric parameters that vary linearly with the temperature, *i.e.*, Δ_1, Δ_2, …, Δ_n, then the temperature can be expressed as a function of each Δ, *i.e.*, $T=f(\Delta_1, \Delta_2, \ldots, \Delta_n)$:

$$T = \beta_0 + \beta_1\Delta_1 + \cdots + \beta_n\Delta_n + \varepsilon = \beta_0 + \sum_{i=1}^{n} \beta_i\Delta_i + \varepsilon \qquad (\mathbf{1})$$

where β_0 is the intercept, β_i (i=1,…, n) is the slope of each thermometric parameter Δ_i (explanatory variable i), and ε is the residual.[66] Henceforth, one can rewrite S_r (details in Section S2.2, Supporting Information):

$$S_r = \sqrt{\sum_{i=1}^{n} \left(\frac{1}{\Delta_i}\left|\frac{\partial \Delta_i}{\partial T}\right|\right)^2} = \sqrt{\sum_{i=1}^{n} \left(\Delta_i \left|\frac{\partial T}{\partial \Delta_i}\right|\right)^{-2}} \qquad (\mathbf{2})$$

Because the model is linear, the relative thermal sensitivity depends on each thermometric parameter taken into account (Δ_i) and its respective slope (β_i), and thus:

$$S_r = \sqrt{\sum_{i=1}^{n} (\Delta_i\beta_i)^{-2}} \qquad (\mathbf{3})$$

The MLR was applied to the EGFP data considering the five distinct Δ_i parameters previously defined and the correlation between the temperature measured with a K-type thermocouple and the temperature obtained from MLR is presented in **Figure 2** (see Section

S2.4, Supporting Information, for further information). By combining all the parameters, S_m reaches 3.0 %·K^{-1}, which represents a 10-fold increase compared to the highest S_m obtained in single parametric sensing of EGFP (0.3 %·K^{-1} for W_1). An improved sensitivity obtained through MLR is observed since the model considers the weighted contribution of each temperature-dependent light emission of EGFP (*i.e.*, each Δ_i), therefore reducing the uncertainties provided by measurements of the temperature based on individual Δ. This is well demonstrated by the measurement of consecutive heating and cooling cycles (**Figure 3**), where the thermal transient curves obtained by luminescence thermometry in Figure 3a-e tend to deviate from the curve measured by a K-type reference thermocouple (this is much more evident for W_2 and I_R). The histograms of the temperature deviation (ΔT) are presented in Figure S11 (Supporting Information) and the results show that MLR provides a lower temperature deviation in Figure 3f because the uncertainties from each Δ_i were already reduced in the model, validating the improved performance of MLR in multiparametric nanothermometry.

Beyond the giant improvement in the relative thermal sensitivity, this novel approach allows achieving more reliable and accurate thermal readouts without requiring the development of new materials, the upgrade of the detection system, or further time-consuming measurements over long integration times. This last makes, for instance, possible to perform time-resolved measurements *in vitro* and *in vivo*.

2.2. Revisiting *in vivo* measurements using Ag_2S nanoparticles

Despite the utility of fluorescent proteins, the novelty of MLR is not limited to luminescent organic compounds, but it can be also applied to inorganic nanoparticles with multi-parametric thermal sensing capabilities. We here, indeed, explore the application of MLR to Ag_2S nanoparticles. Ag_2S nanoparticles possess a unique combination of properties that makes them exceptional for *in vivo* thermal sensing. They operate in the second biological window (infrared

spectral range from 1000 to 1400 nm where tissues become partially transparent[67]) so that they allow for real sub-tissue thermal sensing. Ag_2S nanoparticles show excellent *in vivo* biocompatibility thanks to their good physical-chemical stability.[43,68,69] The emission band of Ag_2S nanoparticles centered at 1200 nm shows a strong temperature dependence and it has been widely reported how a reduced temperature change around room temperature induces relevant changes in the band shape. These temperature-induced changes have been largely used for thermal reading by analyzing either the peak wavelength or the ratio between the emitted intensities at 1175 and 1260 nm. The use of these two thermometric parameters has made possible reliable thermal reading with modest thermal sensitivities at 310 K ranging from 0.1 to 5.0 $\%\cdot K^{-1}$ (**Table 2**).[43] As a consequence of these "modest" thermal sensitivities, the thermal uncertainty achieved by Ag_2S nanothermometers during *in vivo* experiments is not better than 0.5 degrees.[43] The temperature dependence of both intensity ratio and peak energy of emission band corresponding to Ag_2S nanoparticles is presented in **Figure 4**, leading to relative thermal sensitivities of 2.0 and 0.10 $\%\cdot K^{-1}$, respectively. Hereafter we will focus our attention on these two thermoresponsive parameters as they both display a quasi-linear trend, making them amenable for MLR analysis.

Applying the MLR to the Ag_2S data (giving the relative contributions indicated in Figure 4c), we obtained a calibration curve that depends linearly on the peak energy and intensity ratio parameters with a relative thermal sensitivity up to 50 $\%\cdot K^{-1}$ (Figure 4d) This constitutes a 10-fold improvement when compared to that previously reported for Ag_2S nanoparticles and 4 times greater than the greatest S_m value reported so far (12.5 % K^{-1} at 293 K, from a lanthanide metal-organic network, using the intensity ratio approach).[33,43] The performance, in terms of S_r and δT, achieved by combining linear regression to the multiparametric reading of Ag_2S nanothermometers is shown in Figure 4e,f. It is evidenced how the use of linear regression procedures makes it possible to drive the thermal uncertainties provided by Ag_2S nanothermometers well below 1.0 K.

The MLR-induced thermal sensitivity enhancement of Ag_2S nanothermometers opens the possibility of improving the thermal resolution of *in vivo* measurements. In recent work, intratumoral thermal transients were measured by analyzing the time evolution of the infrared emission generated by Ag_2S nanoparticles allocated inside a melanoma tumor during laser irradiation. The different intratumoral thermal readings provided by the different thermometric parameters (emission intensity, peak wavelength, and intensity ratio) were used to assess the reliability of measurements but not to improve the accuracy of the final intratumoral readout. The intratumoral emission spectra generated by Ag_2S nanoparticles were re-analyzed by MLR and the new intratumoral thermal transients during photothermal treatment are shown in **Figure 5** (the thermal transients obtained by using the individual calibration curves are also included for comparison). We identify slight differences in the temperature profiles during the transient regime that are explained by the distinct thermal sensitivity provided by each parameter and are within the temperature uncertainty of each thermometric parameter. Moreover, the intratumoral temperature values calculated from MLR are almost coincident with those provided by the sole analysis of peak energy which, at first glance does not justify the effort of using MLR. The improved performance of MLR is, however, reflected in both S_r and δT values calculated from each thermometric parameter (Figure 5b and Table 2). The intensity ratio allows a temperature determination with uncertainty values ranging from 1.1 to 2.1 K (the lower the sensitivity the higher the temperature uncertainty), and the peak energy improves this value roughly by one order of magnitude ($\delta T \approx 0.15$ K). Finally, the MLR approach renders temperature uncertainties between 0.05 and 0.1 K, which represents an improvement of more than 20 times with respect to that obtained with the intensity ratio. Note that recent perspective articles pointed out that the real use of luminescence thermometry at the clinical level would require achieving thermal resolutions during *in vivo* experiments better than 0.1 degrees.[11] This objective is, then, reached in this work. As a matter of fact, we demonstrate how MLR converts Ag_2S nanoparticles into ultra-sensitive nanothermometers making them a unique system for *in vivo* detection, for

instance, of brain diseases through precise and remote thermal sensing. Once again, it should be highlighted that such improvement for *in vivo* thermal uncertainty has been achieved without requiring any change in the experimental setup or sample preparation.

3. Conclusion

Several strategies are been used to improve the reliability and accuracy of luminescent nanothermometers, namely the combination of different emitting centers[70,71] or the simultaneous assessment of the temperature via several thermometric parameters.[43,72] This work demonstrates that any luminescent thermometer presenting a linear correlation of the distinct thermometric parameters with the temperature can be used to achieve higher sensitivity and lower temperature uncertainty through MLR. We demonstrate the potential of the synergy between MRL and luminescent nanothermometry in two of the most promising systems for thermal sensing in biomedicine: GFPs and Ag_2S nanoparticles. The combination of MLR and the multiparametric thermal readout of EGFP leads to a significant increase of its thermal sensitivity, with a 10-fold improvement. MLR has been also found to improve the relative thermal sensitivity of intratumoral Ag_2S multiparametric nanothermometers by one order of magnitude, reaching a world record of 50 $\%\cdot K^{-1}$. Moreover, the re-analysis of *in vivo* results by using MLR have also demonstrated how is possible to drive the thermal accuracy of *in vivo* measurements well below 0.1 degrees, starting a new era of luminescent nanothermometry at the pre-clinical level.

These results support that MLR is a valid and easily implementable strategy, paving the way for reaching a temperature resolution below 0.1 degrees without further upgrade of the detection systems or materials design, an important step forward for the spread of luminescent nanothermometers as a tool for broader diverse scientific proposes.

4. Experimental Section

Photoluminescence spectroscopy: The emission spectra of EGFP were recorded in the right-angle experimental set-up shown in Figure S2 (Supporting Information). The excitation of the sample was carried out at 408 ± 7 nm with a power density of 0.01 W cm^{-2} by using a CW multi-channel LED light source (MCLS, Sandhouse Design). The excitation source was collimated twice by attaching an adjustable collimator to the tip of the optical fiber and placing a plano-convex lens (LA1145-AB, Thorlabs) between the optical fiber and the sample. The light emission was registered by a USB-portable spectrometer (Maya 2000 Pro, Ocean Optics) coupled to an optical fiber (QP450-1-XSR, Ocean Optics) using an edge pass filter (FESH0750, Thorlabs) to cut off the excitation signal during the spectral acquisition. A high-precision quartz cuvette (QS, 114F-10-40, Hellma Analytics) was filled with 0.50 mL of the EGFP aqueous suspension to perform the measurements.

Thermal calibration: The temperature-dependent measurements using the setup described above and a temperature-controlled cuvette holder (Luma 40, Quantum Northwest) with a temperature controller (TC1, Quantum Northwest) using a water circulator (Bath 10, Quantum Northwest) for heating and cooling the sample. The calibration of temperature was performed with a K-type thermocouple with a temperature uncertainty of 0.1 K (KA01-3, TME Thermometers) coupled to a thermocouple data logger (TC-08, Pico Technology).

Cloning of EGFP: The gene of EGFP containing BamHI and HindIII restriction sites at 5' and 3' ends of the sequence, respectively, was prepared by polymerase chain reaction (PCR). The pQE9 vector containing the BamHI/HindIII restriction sites and the gene encoding for EGFP was purified through a spin column purification and ligated at 3:1 insert to vector molar ratio.

Protein expression and purification: The EGFP plasmid was transformed into *Escherichia coli* strain Tuner (DE3) and the expression of the protein was carried out in Luria Broth (LB), where the cells were grown to OD_{600} = 0.8-1.0 at 310 K before induction. The protein expression was induced by the addition of isopropyl-β-D-1-thiogalactopyranoside (IPTG, 0.5 mmol L^{-1}) and a temperature drop to 303 K. The cells were harvested by centrifugation 18-24 h after induction and resuspended in lysis buffer (NaH_2PO_4 = 50 mmol L^{-1}, NaCl = 300 mmol L^{-1}, imidazole = 10 mmol L^{-1} in water, pH = 8.0). The obtained lysates were stored at 193 K. After thawing, lysozyme (1 mg mL^{-1}) was added to resuspended cells, and the cells were incubated at 277 K for 1 h. The resuspended cells were sonicated with a tip probe and clarified by centrifugation (12,400 rpm) at 277 K. The obtained EGFP aqueous suspension was purified by Ni-NTA affinity chromatography (Ni-NTA Agarose, Qiagen) under native conditions and fast protein liquid chromatography (FPLC) at pH = 8.0. FPLC purification was performed using an anion exchange chromatography column (HiTrap Q HP, GE Life Sciences) under 30 column volumes elution with an increasing linear gradient of NaCl concentration from 0 to 2 mol L^{-1}. The suspension of the protein was dialyzed against ultrapure water and the purity of each protein was confirmed by denaturing

gel electrophoresis (SDS-PAGE). The resulting EGFP aqueous suspension was diluted in tris buffer at pH = 8.0 and stored at 277 K. The confirmed amino acid sequence of the obtained EGFP is presented in Figure S6 of Supporting Information.

Colloidal characterization: The hydrodynamic size (diameter, *d*) of EGFP was measured by dynamic light scattering (DLS) in a Malvern Zetasizer Nano series instrument (Nano-ZS Model ZEN3600, Red badge operating with a 632.8 nm laser) at 298 K. The measurement of the zeta potential (ζ) was carried out in the same equipment by using the Smoluchowski model to analyze the colloidal stability of EGFP in aqueous suspension (0.25 mg mL^{-1} in 20 mmol L^{-1} Tris-Cl, pH = 8.00 ± 0.01). The EGFP sample was measured in a folded capillary cell (DTS1070, Malvern Instruments) for both DLS and zeta potential measurements. Three measurements were performed with ten scans each, where the average values are reported in Figure S7 (Supporting Information).

UV-Vis absorption spectroscopy. The ultraviolet-visible (UV-Vis) absorption spectrum of the EGFP aqueous solution was recorded in a spectrophotometer (Cary 50, Varian) at 293 K with a spectral resolution of 0.5 nm using a 10 mm pathlength quartz cuvette (Figure S8, Supporting Information).

References

1. Martin, G. A Definition of Temperature. *Nature* **73**, 390–390 (1906).
2. Gilman, S. E., Wethey, D. S. & Helmuth, B. Variation in the sensitivity of organismal body temperature to climate change over local and geographic scales. *Proc. Natl. Acad. Sci.* **103**, 9560–9565 (2006).
3. Rosso, L., Tabandeh, S., Beltramino, G. & Fernicola, V. Validation of phosphor thermometry for industrial surface temperature measurements. *Meas. Sci. Technol.* **31**, 034002 (2020).
4. Piñol, R. *et al.* Real-Time Intracellular Temperature Imaging Using Lanthanide-Bearing Polymeric Micelles. *Nano Lett.* **20**, 6466–6472 (2020).
5. Brites, C. D. S. *et al.* Thermometry at the nanoscale. *Nanoscale* **4**, 4799 (2012).
6. Jaque, D. & Vetrone, F. Luminescence nanothermometry. *Nanoscale* **4**, 4301 (2012).
7. Brites, C. D. S., Balabhadra, S. & Carlos, L. D. Lanthanide-Based Thermometers: At the Cutting-Edge of Luminescence Thermometry. *Adv. Opt. Mater.* **7**, 1801239 (2019).
8. Bednarkiewicz, A., Marciniak, L., Carlos, L. D. & Jaque, D. Standardizing luminescence nanothermometry for biomedical applications. *Nanoscale* **12**, 14405–14421 (2020).
9. Dramićanin, M. Schemes for Temperature Read-Out From Luminescence. in *Luminescence Thermometry* (ed. Dramićanin, M.) 63–83 (Elsevier, 2018). doi:10.1016/B978-0-08-102029-6.00004-X.
10. Suta, M. & Meijerink, A. A Theoretical Framework for Ratiometric Single Ion Luminescent Thermometers—Thermodynamic and Kinetic Guidelines for Optimized Performance. *Adv. Theory Simulations* **3**, 2000176 (2020).
11. Zhou, J., del Rosal, B., Jaque, D., Uchiyama, S. & Jin, D. Advances and challenges for fluorescence nanothermometry. *Nat. Methods* **17**, 967–980 (2020).
12. Uchiyama, S., Kawai, N., De Silva, A. P. & Iwai, K. Fluorescent Polymeric AND Logic Gate with Temperature and pH as Inputs. *J. Am. Chem. Soc.* **126**, 3032–3033 (2004).

13. Gota, C., Okabe, K., Funatsu, T., Harada, Y. & Uchiyama, S. Hydrophilic fluorescent nanogel thermometer for intracellular thermometry. *J. Am. Chem. Soc.* **131**, 2766–2767 (2009).
14. Paviolo, C., Clayton, A. H. A., Mcarthur, S. L. & Stoddart, P. R. Temperature measurement in the microscopic regime: A comparison between fluorescence lifetime- and intensity-based methods. *J. Microsc.* **250**, 179–188 (2013).
15. Savchuk, O. A., Silvestre, O. F., Adão, R. M. R. & Nieder, J. B. GFP fluorescence peak fraction analysis based nanothermometer for the assessment of exothermal mitochondria activity in live cells. *Sci. Rep.* **9**, 7535 (2019).
16. McLaurin, E. J., Vlaskin, V. A. & Gamelin, D. R. Water-Soluble Dual-Emitting Nanocrystals for Ratiometric Optical Thermometry. *J. Am. Chem. Soc.* **133**, 14978–14980 (2011).
17. Kalytchuk, S., Zhovtiuk, O., Kershaw, S. V., Zbořil, R. & Rogach, A. L. Temperature-Dependent Exciton and Trap-Related Photoluminescence of CdTe Quantum Dots Embedded in a NaCl Matrix: Implication in Thermometry. *Small* **12**, 466–476 (2016).
18. Brites, C. D. S. *et al.* Simultaneous Measurement of the Emission Quantum Yield and Local Temperature: The Illustrative Example of SrF 2 :Yb 3+ /Er 3+ Single Crystals. *Eur. J. Inorg. Chem.* **2020**, 1555–1561 (2020).
19. Hazra, C., Skripka, A., Ribeiro, S. J. L. & Vetrone, F. Erbium Single-Band Nanothermometry in the Third Biological Imaging Window: Potential and Limitations. *Adv. Opt. Mater.* **2001178**, 2001178 (2020).
20. Brites, C. D. S. *et al.* Instantaneous ballistic velocity of suspended Brownian nanocrystals measured by upconversion nanothermometry. *Nat. Nanotechnol.* **11**, 851–856 (2016).
21. Ximendes, E. C. *et al.* Unveiling in Vivo Subcutaneous Thermal Dynamics by Infrared Luminescent Nanothermometers. *Nano Lett.* **16**, 1695–1703 (2016).
22. Peng, H. *et al.* Luminescent Europium(III) Nanoparticles for Sensing and Imaging of Temperature in the Physiological Range. *Adv. Mater.* **22**, 716–719 (2010).
23. Sójka, M. *et al.* Bandgap Engineering and Excitation Energy Alteration to Manage Luminescence Thermometer Performance. The Case of Sr 2 (Ge,Si)O 4 :Pr 3+. *Adv. Opt. Mater.* **7**, 1901102 (2019).
24. Suta, M. *et al.* Making Nd3+ a Sensitive Luminescent Thermometer for Physiological Temperatures—An Account of Pitfalls in Boltzmann Thermometry. *Nanomaterials* **10**, 543 (2020).
25. Han, Q., Wu, W., Liu, W. & Yang, Y. The peak shift and evolution of upconversion luminescence from CsPbBr 3 nanocrystals under femtosecond laser excitation. *RSC Adv.* **7**, 35757–35764 (2017).
26. Lu, H. *et al.* Ultranarrow NIR bandwidth and temperature sensing of YOF:Yb3+/Tm3+ phosphor in low temperature range. *J. Lumin.* **206**, 613–617 (2019).
27. Laia, A. S. *et al.* Comparing the performance of Nd3+-doped LiBaPO4 phosphors as optical temperature sensors within the first biological window exploiting luminescence intensity ratio and bandwidth methods. *J. Lumin.* **227**, 117524 (2020).
28. Donner, J. S., Thompson, S. A., Kreuzer, M. P., Baffou, G. & Quidant, R. Mapping Intracellular Temperature Using Green Fluorescent Protein. *Nano Lett.* **12**, 2107–2111 (2012).
29. Kong, M. *et al.* Luminescence interference-free lifetime nanothermometry pinpoints in vivo temperature. *Sci. China Chem.* (2021) doi:10.1007/s11426-020-9948-8.
30. Jia, M., Sun, Z., Zhang, M., Xu, H. & Fu, Z. What determines the performance of lanthanide-based ratiometric nanothermometers? *Nanoscale* **12**, 20776–20785 (2020).
31. Nexha, A., Carvajal, J. J., Pujol Baiges, M. C., Díaz, F. & Aguiló, M. Lanthanide doped luminescence nanothermometers in the biological windows: strategies and applications.

Nanoscale DOI: 10.1039/D0NR09150B (2021) doi:10.1039/D0NR09150B.
32. Collins, S. F. *et al.* Comparison of fluorescence-based temperature sensor schemes: Theoretical analysis and experimental validation. *J. Appl. Phys.* **84**, 4649–4654 (1998).
33. Zhao, D. *et al.* 808 nm-Light-Excited Near-Infrared Luminescent Lanthanide Metal–Organic Frameworks for Highly Sensitive Physiological Temperature Sensing. *Chem. – A Eur. J.* **26**, 3145–3151 (2020).
34. Jaque, D. *et al.* Nanoparticles for photothermal therapies. *Nanoscale* **6**, 9494–9530 (2014).
35. Cunha, J. *et al.* Controlling Light, Heat, and Vibrations in Plasmonics and Phononics. *Adv. Opt. Mater.* **8**, 2001225 (2020).
36. Suzuki, M. & Plakhotnik, T. The challenge of intracellular temperature. *Biophys. Rev.* **12**, 593–600 (2020).
37. Lifante, J. *et al.* Reaching Deeper: Absolute In Vivo Thermal Reading of Liver by Combining Superbright Ag 2 S Nanothermometers and In Silico Simulations. *Adv. Sci.* **2003838**, 2003838 (2021).
38. Bednarkiewicz, A. *et al.* Luminescence based temperature bio-imaging: Status, challenges, and perspectives. *Appl. Phys. Rev.* **8**, 011317 (2021).
39. Jiang, Y. *et al.* A three-mode self-referenced optical thermometry based on up-conversion luminescence of Ca2MgWO6:Er3+,Yb3+ phosphors. *Chem. Eng. J.* **413**, 127470 (2021).
40. Liu, J., Yue, X., Wang, Z., Zhang, X. & Xu, Y. Coumarin 7 functionalized europium-based metal–organic-framework luminescent composites for dual-mode optical thermometry. *J. Mater. Chem. C* **8**, 13328–13335 (2020).
41. Marciniak, L., Elzbieciak-Piecka, K., Kniec, K. & Bednarkiewicz, A. Assessing thermometric performance of Sr2CeO4 and Sr2CeO4:Ln3+ (Ln3+ = Sm3+, Ho3+, Nd3+, Yb3+) nanocrystals in spectral and temporal domain. *Chem. Eng. J.* **388**, 124347 (2020).
42. Brites, C. D. S., Martínez, E. D., Urbano, R. R., Rettori, C. & Carlos, L. D. Self-Calibrated Double Luminescent Thermometers Through Upconverting Nanoparticles. *Front. Chem.* **7**, 1–10 (2019).
43. Shen, Y. *et al.* Ag 2 S Nanoheaters with Multiparameter Sensing for Reliable Thermal Feedback during In Vivo Tumor Therapy. *Adv. Funct. Mater.* **2002730**, 2002730 (2020).
44. Santos, H. D. A. *et al.* Ultrafast photochemistry produces superbright short-wave infrared dots for low-dose in vivo imaging. *Nat. Commun.* **11**, 2933 (2020).
45. Day, R. N. & Davidson, M. W. The fluorescent protein palette: tools for cellular imaging. *Chem. Soc. Rev.* **38**, 2887 (2009).
46. Silva, P. L. *et al.* Mapping intracellular thermal response of cancer cells to magnetic hyperthermia treatment. *Nanoscale* (2020) doi:10.1039/C9NR10370H.
47. Lambert, G. G. *et al.* Aequorea's secrets revealed: New fluorescent proteins with unique properties for bioimaging and biosensing. *PLOS Biol.* **18**, e3000936 (2020).
48. Kiyonaka, S. *et al.* Genetically encoded fluorescent thermosensors visualize subcellular thermoregulation in living cells. *Nat. Methods* **10**, 1232–1238 (2013).
49. Liang, S. *et al.* An ultrasensitive ratiometric fluorescent thermometer based on frustrated static excimers in the physiological temperature range. *Chem. Commun.* **55**, 3509–3512 (2019).
50. Mi, C., Zhou, J., Wang, F., Lin, G. & Jin, D. Ultrasensitive Ratiometric Nanothermometer with Large Dynamic Range and Photostability. *Chem. Mater.* **31**, 9480–9487 (2019).
51. Nathans, L. L., Oswald, F. L. & Nimon, K. Interpreting multiple linear regression: A guidebook of variable importance. *Pract. Assessment, Res. Eval.* **17**, 1–19 (2012).
52. Elshendy, M., Colladon, A. F., Battistoni, E. & Gloor, P. A. Using four different online

media sources to forecast the crude oil price. *J. Inf. Sci.* **44**, 408–421 (2018).
53. Abraham, J., Higdon, D. & Nelson, J. Cryptocurrency price prediction using tweet volumes and sentiment analysis. *SMU Data Sci. Rev.* **1**, 22 (2018).
54. Buntain, C. & Golbeck, J. Automatically Identifying Fake News in Popular Twitter Threads. in *2017 IEEE International Conference on Smart Cloud (SmartCloud)* 208–215 (IEEE, 2017). doi:10.1109/SmartCloud.2017.40.
55. McGregor, S. C., Mourão, R. R. & Molyneux, L. Twitter as a tool for and object of political and electoral activity: Considering electoral context and variance among actors. *J. Inf. Technol. Polit.* **14**, 154–167 (2017).
56. Wang, J. *et al.* Multiple Linear Regression and Artificial Neural Network to Predict Blood Glucose in Overweight Patients. *Exp. Clin. Endocrinol. Diabetes* **124**, 34–38 (2016).
57. Ma, J. *et al.* Assessment of triglyceride and cholesterol in overweight people based on multiple linear regression and artificial intelligence model. *Lipids Health Dis.* **16**, 42 (2017).
58. Creek, D. J. *et al.* Toward Global Metabolomics Analysis with Hydrophilic Interaction Liquid Chromatography–Mass Spectrometry: Improved Metabolite Identification by Retention Time Prediction. *Anal. Chem.* **83**, 8703–8710 (2011).
59. Fernández-Fernández, M. *et al.* Simultaneous Determination of Creatinine and Creatine in Human Serum by Double-Spike Isotope Dilution Liquid Chromatography–Tandem Mass Spectrometry (LC-MS/MS) and Gas Chromatography–Mass Spectrometry (GC-MS). *Anal. Chem.* **87**, 3755–3763 (2015).
60. dos Santos, A. M. Thermal Effect on Aequorea Green Fluorescent Protein Anionic and Neutral Chromophore Forms Fluorescence. *J. Fluoresc.* **22**, 151–154 (2012).
61. Jacchetti, E., Gabellieri, E., Cioni, P., Bizzarri, R. & Nifosì, R. Temperature and pressure effects on GFP mutants: explaining spectral changes by molecular dynamics simulations and TD-DFT calculations. *Phys. Chem. Chem. Phys.* **18**, 12828–12838 (2016).
62. Beechem, T., Christensen, A., Graham, S. & Green, D. Micro-Raman thermometry in the presence of complex stresses in GaN devices. *J. Appl. Phys.* **103**, 124501 (2008).
63. Saltonstall, C. B., Serrano, J., Norris, P. M., Hopkins, P. E. & Beechem, T. E. Single element Raman thermometry. *Rev. Sci. Instrum.* **84**, 064903 (2013).
64. Maestro, L. M. *et al.* CdSe Quantum Dots for Two-Photon Fluorescence Thermal Imaging. *Nano Lett.* **10**, 5109–5115 (2010).
65. Rocha, U. *et al.* Subtissue Thermal Sensing Based on Neodymium-Doped LaF 3 Nanoparticles. *ACS Nano* **7**, 1188–1199 (2013).
66. Olive, D. J. *Linear Regression*. *Linear Regression* (Springer International Publishing, 2017). doi:10.1007/978-3-319-55252-1.
67. Hemmer, E., Benayas, A., Légaré, F. & Vetrone, F. Exploiting the biological windows: current perspectives on fluorescent bioprobes emitting above 1000 nm. *Nanoscale Horizons* **1**, 168–184 (2016).
68. Zhang, Y. *et al.* Ag 2 S Quantum Dot: A Bright and Biocompatible Fluorescent Nanoprobe in the Second Near-Infrared Window. *ACS Nano* **6**, 3695–3702 (2012).
69. del Rosal, B. *et al.* In Vivo Contactless Brain Nanothermometry. *Adv. Funct. Mater.* **28**, 1806088 (2018).
70. Qiu, X. *et al.* Ratiometric upconversion nanothermometry with dual emission at the same wavelength decoded via a time-resolved technique. *Nat. Commun.* **11**, 4 (2020).
71. Liu, F. *et al.* An optical thermometer with high sensitivity and superior signal discriminability based on dual-emitting Ce3+/Eu2+ co-doped La5Si2BO13 thermochromic phosphor. *J. Rare Earths* 124658 (2020) doi:10.1016/j.jre.2020.10.003.
72. Marciniak, L., Prorok, K., Francés-Soriano, L., Pérez-Prieto, J. & Bednarkiewicz, A. A broadening temperature sensitivity range with a core–shell YbEr@YbNd double

ratiometric optical nanothermometer. *Nanoscale* **8**, 5037–5042 (2016).
73. Kamei, Y. *et al.* Infrared laser–mediated gene induction in targeted single cells in vivo. *Nat. Methods* **6**, 79–81 (2009).
74. Nakano, M. *et al.* Genetically encoded ratiometric fluorescent thermometer with wide range and rapid response. *PLoS One* **12**, e0172344 (2017).
75. Ruiz, D. *et al.* Ag/Ag 2 S Nanocrystals for High Sensitivity Near-Infrared Luminescence Nanothermometry. *Adv. Funct. Mater.* **27**, 1604629 (2017).
76. Santos, H. D. A. *et al.* Time resolved spectroscopy of infrared emitting Ag 2 S nanocrystals for subcutaneous thermometry. *Nanoscale* **9**, 2505–2513 (2017).
77. Santos, H. D. A. *et al.* In Vivo Early Tumor Detection and Diagnosis by Infrared Luminescence Transient Nanothermometry. *Adv. Funct. Mater.* **28**, 1803924 (2018).

Supporting Information

Supporting Information is available from the Wiley Online Library or from the author.

Acknowledgments

This work was developed within the scope of the projects CICECO-AveiroInstitute of Materials (UIDB/50011/2020 and UIDP/50011/2020) and Shape of Water (PTDC/NAN-PRO/3881/2020) financed by Portuguese funds through the FCT/MEC and when appropriate co-financed by FEDER under the PT2020 Partnership Agreement. This project has received funding from the European Union's Horizon 2020 research and innovation programme under the Marie Sklodowska-Curie Grant Agreement No. 823941. The support of the European Union's Horizon 2020 FET Open program under Grant Agreement No. 801305 (NanoTBTech) is also acknowledged. F.E.M. acknowledges the financial support from the Brazilian agency FAPESP (Process No. 15/50382-2).

Figures

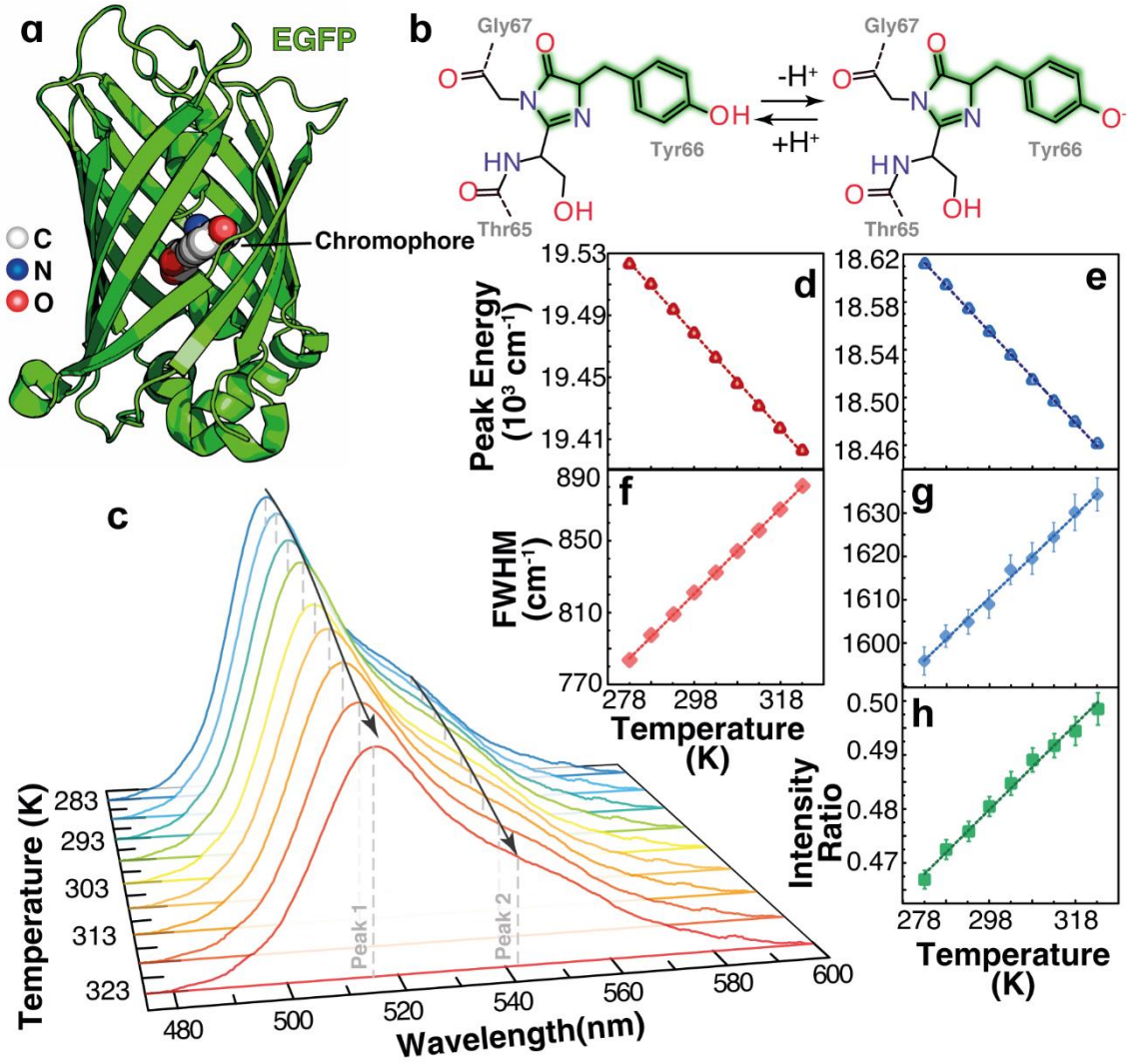

Figure 1. (a) Three-dimensional view of the EGFP structure (based on Protein Data Bank ID 2y0g). (b) Neutral and anionic forms of EGFP chromophore. The amino acid residues are shown close to the anionic form and the optically active part of the chromophore is depicted in a green blur for both forms. (c) Emission spectra of EGFP under excitation at 408 nm at different temperatures. Temperature dependence of the distinct thermometric parameters: (d) E_1, (**e**) E_2, (f) W_1, (g) W_2, and (h) I_R. The lines are the best linear fits of the data to straight lines (r^2>0.99 in all cases). The fit parameters are shown in Table S1 (Supporting Information).

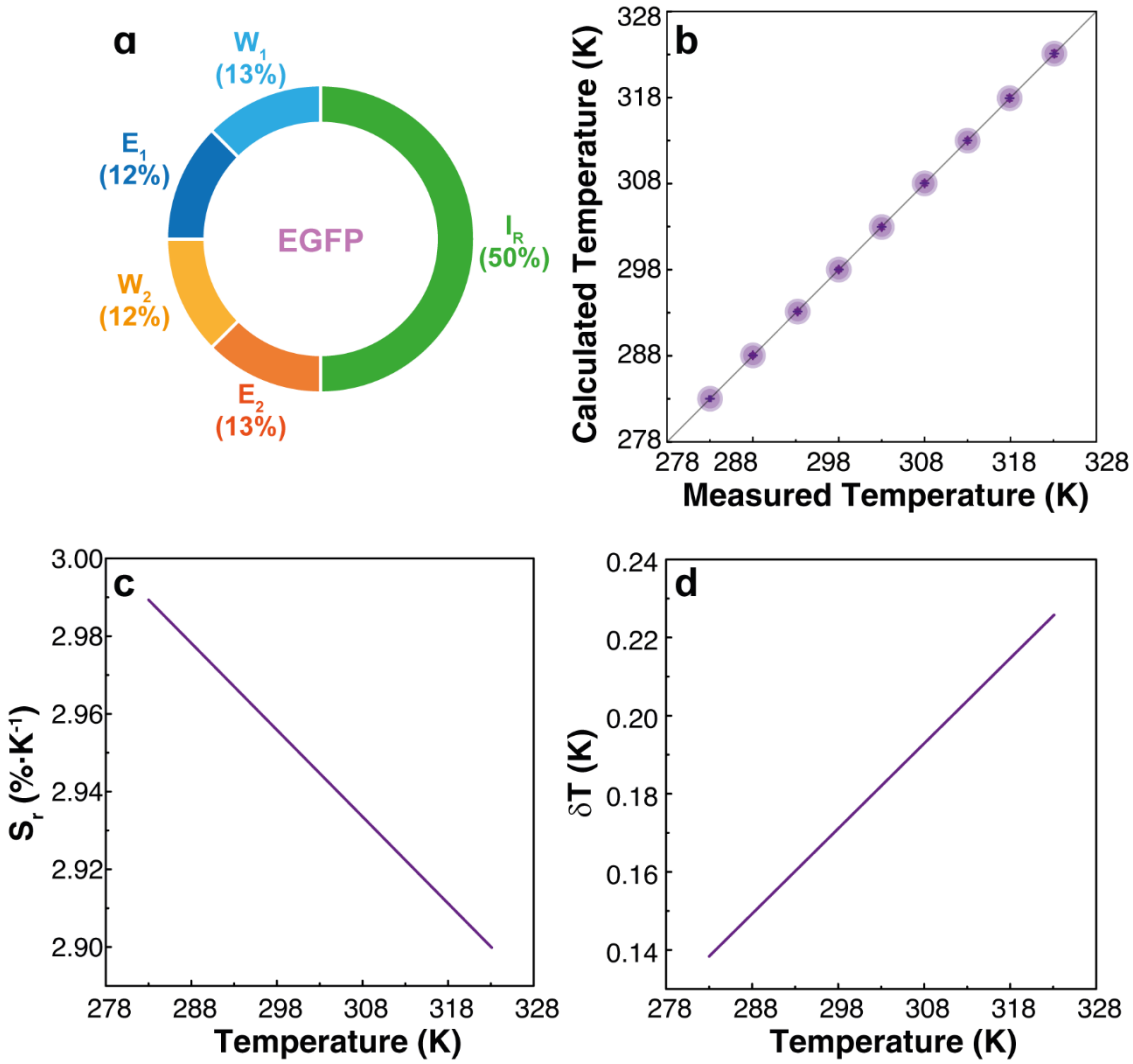

Figure 2. (a) Donut chart of the relative weight (values within parenthesis from β weights) of the distinct thermometric parameters considered for MLR applied to EGFP. (b) Correlation between the temperature measured with the thermocouple (*x*-axis) and the temperature calculated from the combination of all the thermometric parameters from EGFP emission spectra through MLR (*y*-axis). The dashed black lines are guides for the eyes corresponding to $y=x$ (fit parameters are shown in Table S2, Supporting Information). (c) Relative thermal sensitivity and (d) temperature uncertainty of EGFP using MLR.

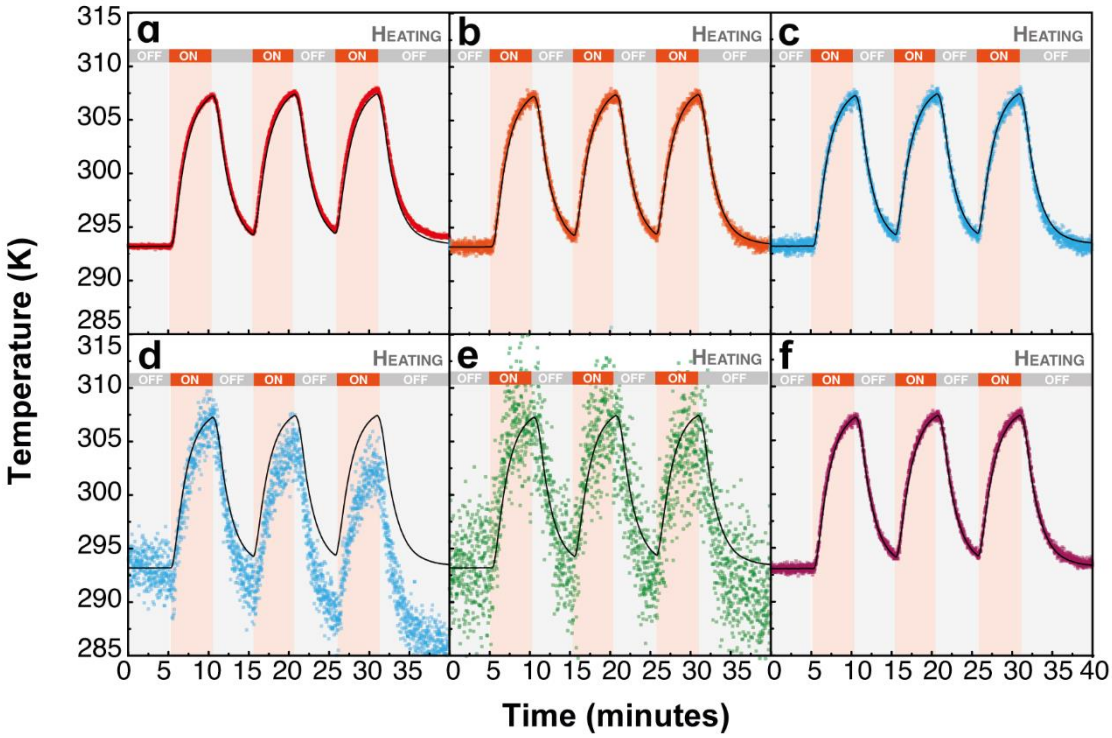

Figure 3. Consecutive heating (red) and cooling (gray) cycles of the EGFP aqueous suspension. The black solid line indicates the measurement of the temperature performed by a reference thermocouple and the symbols the temperature calculated from (a) E_1, (b) E_2, (c) W_1, (d) W_2, (e) I_R, and (f) MLR applied to the EGFP emission spectra. The corresponding histogram of the temperature deviation between the temperature measured with the thermocouple and the temperature calculated using the distinct parameters are presented in Figure S11.

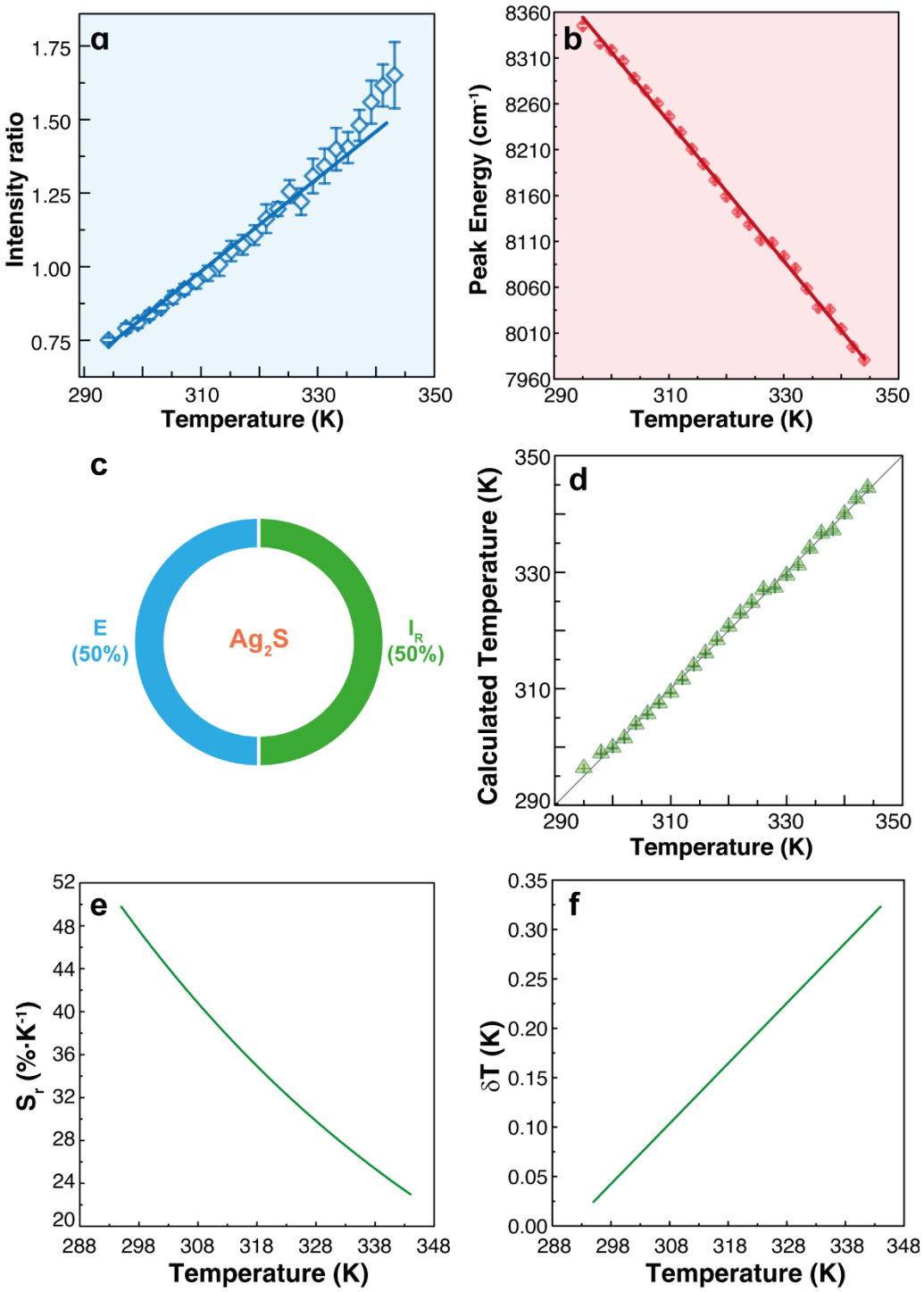

Figure 4. Calibration curves of the Ag_2S NPs using (a) the intensity ratio[43] and (b) the peak energy. The solid lines are the best fits to straight lines (the correlation coefficients and fitting parameters are presented in Table S3, Supporting Information). (c) Donut chart of the relative weight (values within parenthesis from β weights) of the distinct thermometric parameters considered for MLR applied to Ag_2S. (d) Correlation between the temperature measured with the thermocouple (x-axis) and the temperature calculated from the combination of all the thermometric parameters from Ag_2S emission spectra through MLR (y-axis). The dashed black lines are guides for the eyes corresponding to $y=x$ (fit parameters are shown in Supporting Table S4, Supporting Information). Relative thermal sensitivity (e) and temperature uncertainty (f) of Ag_2S using MLR.

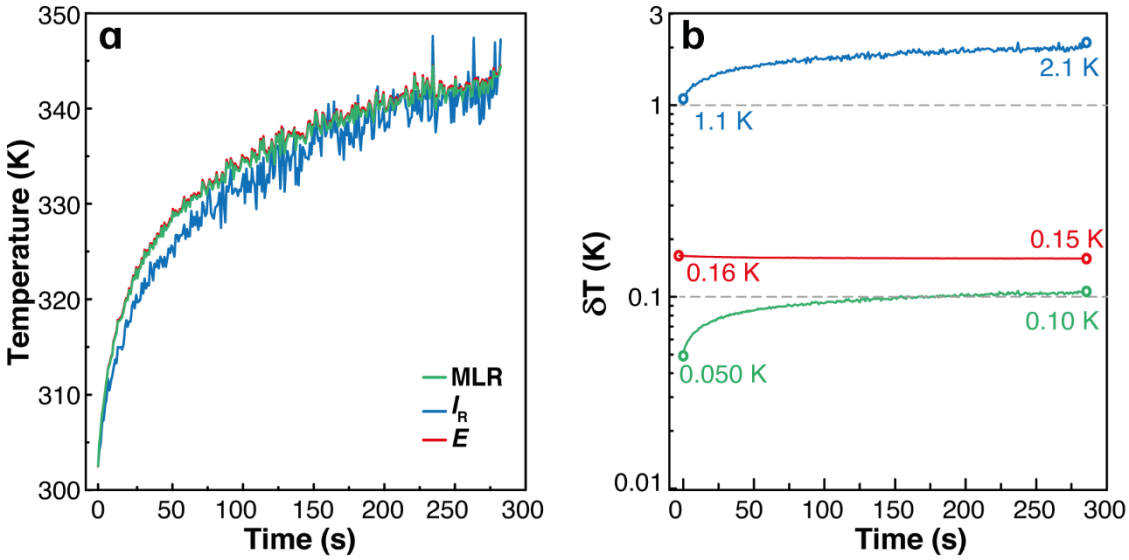

Figure 5. (a) Temporal evolution of the 808 nm laser-induced tumor temperature during photothermal treatment, calculated from the intensity ratio (as reported in ref. [43]), peak energy, and multiple linear regression (partially overlapped, calculated by us). The transient curves were recalculated from the data published elsewhere.[43] (b) The temporal-evolution of the corresponding temperature uncertainties.

Tables

Table 1. Temperature calibration range, maximum relative thermal sensitivity (S_m), and the temperature at which it occurs (T_m) for different GFP-based proteins using multi- and single-parametric analysis.

Protein	Temperature range (K)	S_m (%·K^{-1})	T_m (K)	Method	Reference
EGFP	283 – 323	3.0	283.0	MLR	This work
		0.17	283.0	I_R	
		1.6×10^{-2}	283.0	E	
		2.1×10^{-2}	283.0		
		0.33	283.0	W	
		0.10	283.0		
emGFP-Mito	296 – 312	2.2	296.0	Peak fraction [e]	15
		4.4	312.0	Single intensity [f]	
GFP	293 – 333	2.1	333.0	Single intensity [h]	73
actin-GFP [a]	288 – 343	0.2	302.0	Lifetime [i]	46
tsGFP1 [b]	307 – 314	3.0	314.0	I_R	48
tsGFP2 [c]	311 – 319	3.1	319.0		
gTEMP [d]	278 – 323	2.6	278.0	I_R	74

[a] GFP coupled to actin filaments; [b,c] Fluorophore-forming region of GFP inserted between tandem repeats of the coiled-coil region of TlpA and the full-length TlpA, respectively; [d] Genetically encoded ratiometric fluorescent temperature indicator from Sirius and mT-Sapphire GFP-derived proteins linked by a *Thosea asigna* virus 2A peptide; [e] $(I_1–I_2)/(I_1+I_2)$, where I_1 and I_2 are the integrated emission areas between 495–504 nm and 505–600 nm, respectively (nonlinear dependence); [f] Fluorescence intensity of the peak maximum at around 510 nm under excitation at 488 nm (nonlinear dependence); [g] $(I_{\parallel}–I_{\perp})/(I_{\parallel}+2I_{\perp})$, where $I_{\parallel}$ and $I_{\perp}$ are the intensities of the fluorescence polarized parallel and perpendicular to the incident polarization, respectively; [h] Fluorescence intensity of the peak maximum at around 510 nm under excitation at 473 nm; [i] Emission lifetime under excitation at 467 nm monitoring emission at 510 nm.

Table 2. Temperature calibration range, maximum relative thermal sensitivity (S_m), and the temperature at which it occurs (T_m) for different Ag_2S nanoparticles, using distinct methods.

Nanoparticle	Temperature range (K)	S_m (%·K^{-1})	T_m (K)	Method	Reference
Ag_2S-PEG [a)]	295 – 353	50	295.0	MLR	This work[43]
		9.5×10^{-2}	344.0	E	
Ag_2S-PEG	293 – 353	5.0	295.0	Single intensity [c)]	43
		0.10	295.0	Peak wavelength [d)]	
		2.0	295.0	I_R	
Ag/Ag_2S	288 – 323	8.5	323.0	Single intensity	75
		2.0	323.0	I_R	
Ag_2S-PEG	295 – 323	3.0	295.0	Lifetime [e)]	76
Ag_2S-DDT [b)]		4.0	295.0		
Ag_2S-PEG	299 – 313	3.0	299.0	Single intensity	69
Ag_2S-PEG	293 – 318	3.0	293.0	Single intensity	77

[a)] Nanoparticles functionalized with polyethylene glycol; [b)] Nanoparticles functionalized with 1-dodecane- thiol; [c)] Total integrated emission area (nonlinear dependence); [d)] Wavelength at the maximum intensity of the peak; [e)] Emission lifetime under excitation at 450 nm monitoring emission at the maximum intensity of the peak.